



## Article

# Improving Photoelectrochemical Activity of ZnO/TiO<sub>2</sub> Core–Shell Nanostructure through Ag Nanoparticle Integration

Zeli Wang <sup>1</sup> , Zhen Chen <sup>2</sup>, Jiadong Dan <sup>3</sup>, Weiqiang Chen <sup>2,†</sup>, Chenghang Zhou <sup>3</sup>, Zexiang Shen <sup>2</sup>, Tze Chien Sum <sup>2</sup>  and Xue-Sen Wang <sup>1,\*</sup>

<sup>1</sup> Department of Physics, National University of Singapore, Singapore 117551, Singapore; e0001409@u.nus.edu

<sup>2</sup> School of Physical and Mathematical Sciences, Nanyang Technological University, Singapore 637371, Singapore; chen.zhen@kit.edu (Z.C.); wqchen1990@163.com (W.C.); zexiang@ntu.edu.sg (Z.S.); tzechien@ntu.edu.sg (T.C.S.)

<sup>3</sup> Department of Materials Science and Engineering, National University of Singapore, Singapore 117575, Singapore; jiadong.dan@u.nus.edu (J.D.); zhou\_chenghang@u.nus.edu (C.Z.)

\* Correspondence: phywxs@nus.edu.sg; Tel.: +65-6516-2961

† Current address: MOE Key Laboratory of Laser Life Science & Institute of Laser Life Science, Guangdong Provincial Key Laboratory of Laser Life Science, College of Biophotonics, South China Normal University, Guangzhou 510631, China.

**Abstract:** In solar energy harvesting using solar cells and photocatalysts, the photoexcitation of electrons and holes in semiconductors is the first major step in the solar energy conversion. The lifetime of carriers, a key factor determining the energy conversion and photocatalysis efficiency, is shortened mainly by the recombination of photoexcited carriers. We prepared and tested a series of ZnO/TiO<sub>2</sub>-based heterostructures in search of designs which can extend the carrier lifetime. Time-resolved photoluminescence tests revealed that, in ZnO/TiO<sub>2</sub> core–shell structure the carrier lifetime is extended by over 20 times comparing with the pure ZnO nanorods. The performance improved further when Ag nanoparticles were integrated at the ZnO/TiO<sub>2</sub> interface to construct a Z-scheme structure. We utilized these samples as photoanodes in a photoelectrochemical (PEC) cell and analyzed their solar water splitting performances. Our data showed that these modifications significantly enhanced the PEC performance. Especially, under visible light, the Z-scheme structure generated a photocurrent density 100 times higher than from the original ZnO samples. These results reveal the potential of ZnO-Ag-TiO<sub>2</sub> nanorod arrays as a long-carrier-lifetime structure for future solar energy harvesting applications.

**Keywords:** photocatalysis; carrier lifetime; ZnO/Ag/TiO<sub>2</sub> heterostructure; Z-scheme structure; PEC water splitting



**Citation:** Wang, Z.; Chen, Z.; Dan, J.; Chen, W.; Zhou, C.; Shen, Z.; Sum, T.C.; Wang, X.-S. Improving Photoelectrochemical Activity of ZnO/TiO<sub>2</sub> Core–Shell Nanostructure through Ag Nanoparticle Integration. *Catalysts* **2021**, *11*, 911. <https://doi.org/10.3390/catal11080911>

Academic Editor: Tzu-Hsuan Chiang

Received: 24 June 2021

Accepted: 24 July 2021

Published: 28 July 2021

**Publisher's Note:** MDPI stays neutral with regard to jurisdictional claims in published maps and institutional affiliations.



**Copyright:** © 2021 by the authors. Licensee MDPI, Basel, Switzerland. This article is an open access article distributed under the terms and conditions of the Creative Commons Attribution (CC BY) license (<https://creativecommons.org/licenses/by/4.0/>).

## 1. Introduction

Owing to the rapidly growing demand for energy, and the numerous disastrous energy-related environmental problems in the past several decades, it is imperative to seek for clean and sustainable renewable energy resources. Among all the options, i.e., wind energy, solar energy, nuclear energy, geothermal energy, and hydroelectricity, solar energy plays a very important role in this field [1–5]. In order to efficiently utilize solar energy, various solar energy harvesting routes have been established. For example, photoelectrochemical (PEC) water splitting, a method with advantageous features of producing energy-dense fuel with minimal carbon footprint, has been regarded as a promising approach, which can capture and store renewable solar energy simultaneously [6–8]. The pioneering exploration of PEC can be traced back to 1972, when Fujishima and Honda firstly reported the PEC hydrogen production with titanium dioxide photoelectrode [9]. Since then, intensive efforts have been dedicated to the studies of photo-active catalytic materials. In most of the solar energy harvesting routes, such as solar cells and photocatalysts, semiconductors are the core components of the solar energy conversion devices

based on the photo excitation of electrons and holes in semiconductors to absorb solar energy [7,10–12]. In the field of PEC water splitting, the nanomaterials of low-cost semiconductor metal oxides such as ZnO ( $E_g \approx 3.3$  eV), TiO<sub>2</sub> (band gap  $E_g \approx 3.2$  eV), and Fe<sub>2</sub>O<sub>3</sub> ( $E_g \approx 2.4$  eV) are of particular interest for photocatalysis base materials due to their excellent chemical stability, low cost, safe to environment, and potentially high conversion efficiency [6,10–20].

However, the practically achieved solar energy conversion efficiency of PEC systems based on these semiconductors remains rather low. Besides a relatively large band gap for ZnO and TiO<sub>2</sub>, one of the main factors is the low carrier transfer efficiency due to fast recombination of the photogenerated electrons and holes. To overcome this obstacle, strategies such as heterostructural construction have been employed [21–25]. In the application of PEC water splitting, nanostructured semiconductor photoelectrode possesses a large surface-to-volume ratio (SVR), thus reducing the migration distance of photo-excited carriers and facilitating their transfer to surface. The heterojunctions integrating ZnO or TiO<sub>2</sub> with another semiconductor [26–32] or metal co-catalyst [33–43] have been explored by many researchers. Moreover, heterogeneous structures which combine more than two semiconductors or semiconductor–metal junctions have also been employed as an effective strategy to promote carrier separation, avoid the carrier recombination and improve solar energy conversion efficiency [44–50]. With multiple pathways, these structures efficiently promote the directional transfer of carriers at the interfaces. Consequently, the possibilities of recombination in each semiconductor can be suppressed and the lifetimes of these charge carriers be extended.

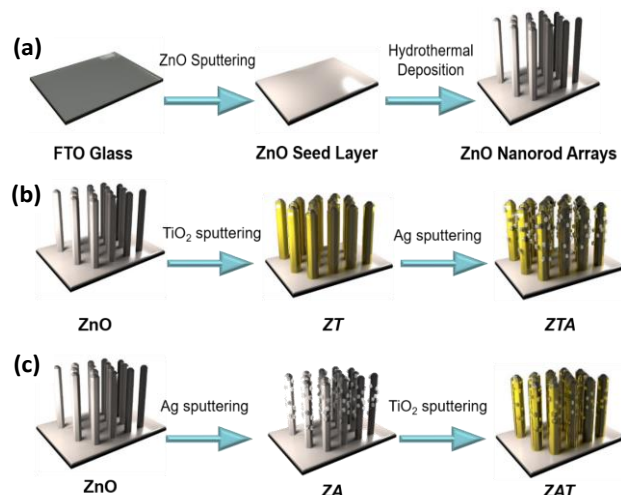
In this study, we synthesized and tested core–shell nanostructures based on hydrothermally synthesized ZnO nanorod arrays. On the ZnO nanorod core, TiO<sub>2</sub> coating layer produced by radio-frequency (RF) sputtering deposition not only can form heterojunction interfaces, but also enhance the surface activity and protect ZnO core during the PEC water splitting process as TiO<sub>2</sub> is more stable than ZnO. Our time-resolved photoluminescence (PL) spectral data demonstrated that the carrier lifetime is dramatically extended by this modification. To further improve the carrier dynamic properties of our samples, we explored the integration silver nanoparticles (Ag NPs) at the ZnO/TiO<sub>2</sub> interfaces to achieve higher carrier separation efficiency and extend the carrier lifetime, taking advantage of localized surface plasmon resonance (LSPR) [42,51–55] or the Z-scheme structure [56–60]. By doing so, the carrier lifetime has indeed been extended further. As an application, we also observed greatly boosted water splitting performance of these modified structures with a visible light source in PEC water splitting test.

## 2. Results and Discussion

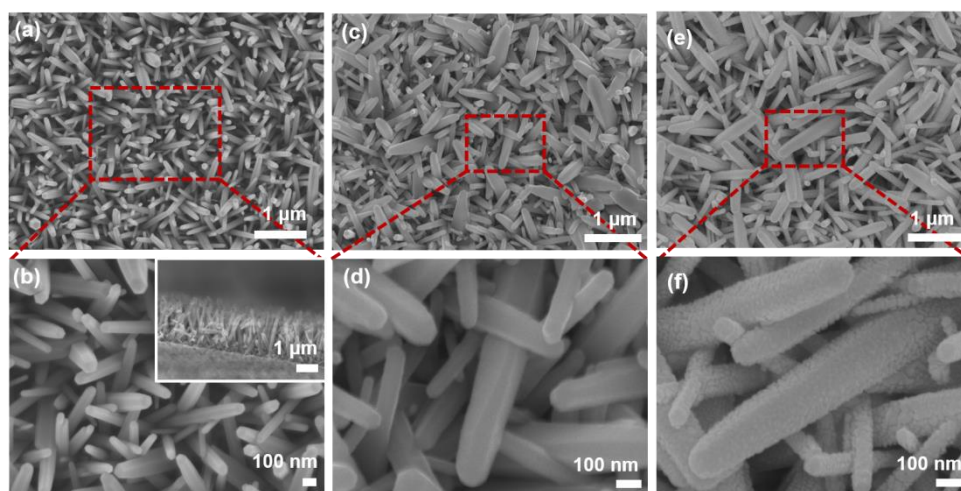
### 2.1. Morphology and Atomic Structure

The PEC and related properties of four types of heterostructures based on ZnO nanorod arrays were investigated in this work. As described in detail in Section 3, our ZnO nanorod arrays were grown on fluorine-doped tin oxide coated (FTO) glass with hydrothermal method [33,61–63], as shown schematically in Figure 1a. TiO<sub>2</sub> was coated on the ZnO nanorods using RF sputtering deposition, forming the ZnO/TiO<sub>2</sub> core–shell structure as shown in Figure 1b, noted as *ZT*. Then, Ag NPs were integrated on the *ZT* core–shell samples, also with RF sputtering deposition, forming ZnO/TiO<sub>2</sub>/Ag (*ZTA*) heterostructures. Alternatively, Ag NPs were formed first on ZnO nanorods arrays through RF sputtering deposition, yielding the ZnO nanorod/Ag NPs (*ZA*) junctions. Then, the *ZA* sample was coated with a TiO<sub>2</sub> layer, giving us the ZnO/Ag/TiO<sub>2</sub> (*ZAT*) heterostructures, as shown in Figure 1c. Figure 2a,b displays the SEM images of the as-synthesized ZnO nanorod arrays on FTO glass. The ZnO nanorods exhibit a diameter roughly in a range of 40 to 200 nm and their height is  $\leq 3$   $\mu$ m (see the inset in Figure 2b). The *ZT* structure as shown in Figure 2c,d inherits the original nanorod morphology. Unlike the pure ZnO, the *ZT* nanorod edges are less sharp, resulting from the TiO<sub>2</sub> coating layer which increases the surface roughness. Due to the relatively big variation in nanorod diameter, it is rather

difficult to obtain the thickness of  $\text{TiO}_2$  coating layer from our scanning electron microscopy (SEM) images. After integrating the Ag NPs at the interface of ZnO and  $\text{TiO}_2$ , the SEM images of **ZAT** structure shown in Figure 2e,f demonstrate highly rough surfaces, which is more clearly visible in Figure 3, indicating successful incorporation of Ag NPs.



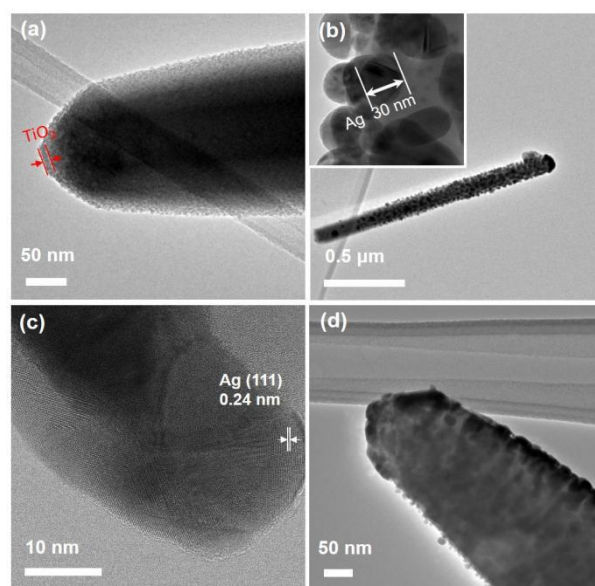
**Figure 1.** Schematics of the synthesize processes of samples based on ZnO nanorod arrays. (a) Hydrothermal growth of ZnO nanorod arrays, (b) **ZT** and **ZTA** structures, and (c) **ZA** and **ZAT** structures.



**Figure 2.** SEM images of (a,b) ZnO nanorod arrays at different magnifications, inset is the cross-sectional view of ZnO nanorod arrays; (c,d) **ZT**; (e,f) **ZAT**.

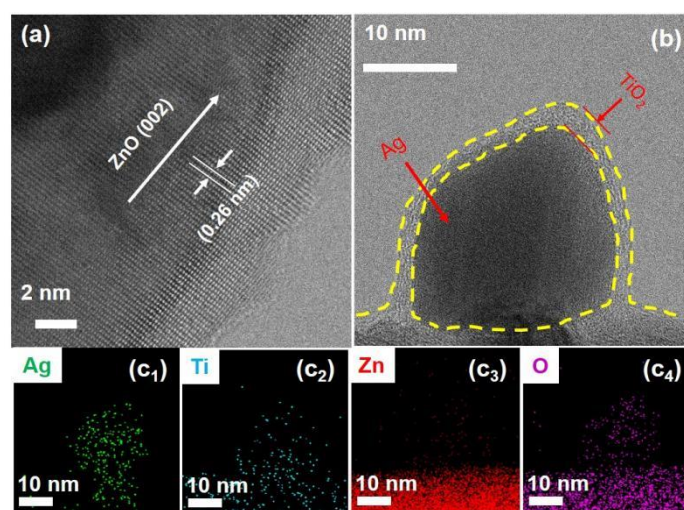
Transmission electron microscopy (TEM) measurement was conducted to get a clear view about the nanorod surface evolution. The thickness of  $\text{TiO}_2$  coated on the ZnO nanorod in Figure 3a is estimated to be 5–10 nm. Our **ZT** core-shell structure is quite different than the structures of ZnO deposited on  $\text{TiO}_2$  nanowires reported by Han et al. [64], which initially formed as nanoscale seeds and later grew as tip-shaped branches.

Figure 3b shows the TEM image of a single as-synthesized ZnO nanorod uniformly integrated with Ag NPs (**ZA**) except near the bottom at the left end, as the sputtered Ag can barely reach this part. According to the inset image of higher magnification, the average diameter of Ag NPs is about 30 nm. The clear fringes shown in Figure 3c can be assigned to the (111) planes of Ag crystal with a layer spacing of 0.24 nm. The TEM image of **ZAT** is shown in Figure 3d. The increased surface roughness due to Ag NP integration in the **ZAT** can be seen by comparing Figure 3a,d.



**Figure 3.** TEM and HRTEM images of (a) tip of a ZT nanorod, (b) single ZA nanorod with the inset image focus on the Ag NPs on its surface, (c) HRTEM image of an Ag NP on the surface of ZA nanorod, and (d) tip of a ZAT nanorod.

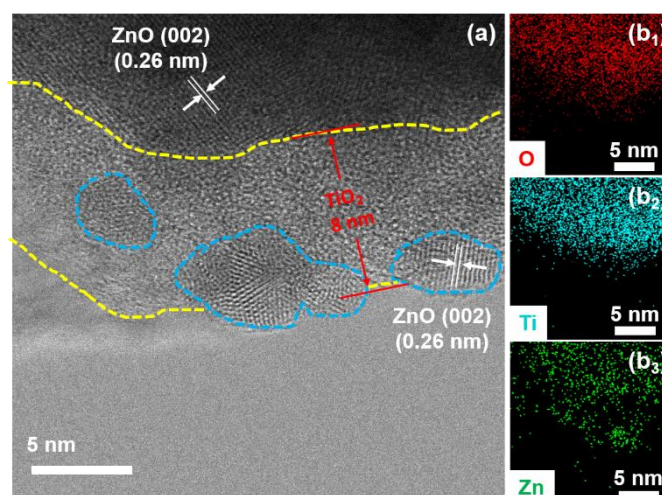
We also performed scanning transmission electron microscopy (STEM) analysis for identifying the structure of ZAT at atomic scale. An exposed ZnO core region was picked purposely from the bottom part of a nanorod to focus on pure ZnO part as shown in Figure 4a. The lattice spacing of 0.26 nm can be indexed to the (002) lattice plane of ZnO [27]. Figure 4b displays an Ag NP at the interface of ZnO core and TiO<sub>2</sub> shell. Unlike the well-crystallized ZnO, the TiO<sub>2</sub> layer remains in amorphous state, probably due to the very small particle size. The TiO<sub>2</sub> layers are well dispersed on the surface of not only ZnO nanorod but also the Ag NPs. This can be further corroborated by the energy dispersive spectroscopy (EDS) mapping results of the same area displayed in Figure 4c. Due to the low probability of X-ray emission for light elements, the EDS signals of Ti and O from the TiO<sub>2</sub> shell is relatively weak. As the EDS signal intensity also depends on the electron beam irradiation time during the STEM imaging, we observe the EDS signals of Ti and O from the TiO<sub>2</sub> shell mainly in the Ag NP area marked in Figure 4b (which is generated from the TiO<sub>2</sub> shell in the front and back sides of the imaged Ag NP), rather than the surrounding thin layer.



**Figure 4.** STEM image focus on (a) exposed ZnO nanorod core and (b) Ag NP at ZnO/TiO<sub>2</sub> interface; EDS mappings of (c<sub>1</sub>) Ag, (c<sub>2</sub>) Ti, (c<sub>3</sub>) Zn, and (c<sub>4</sub>) O.

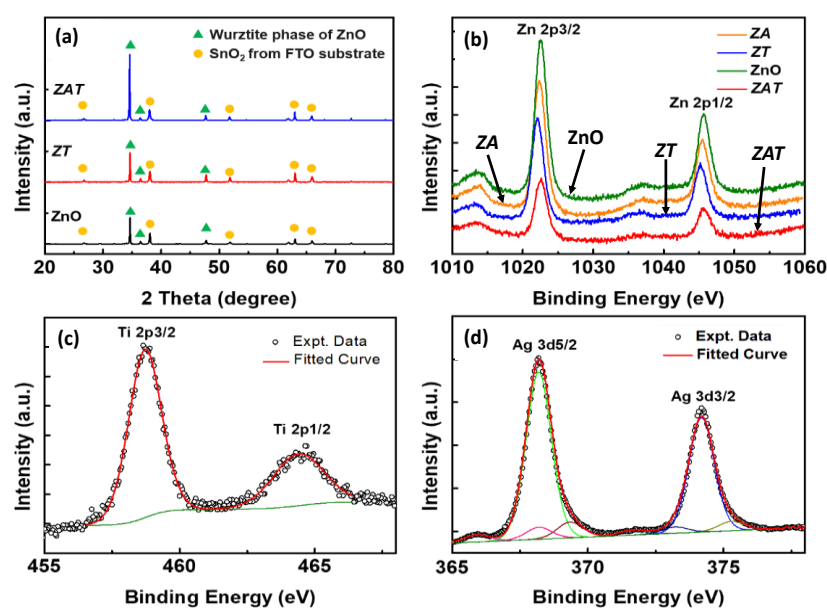


Figure 5 displays STEM mappings taken from a region without Ag NPs. The STEM image in Figure 5a and EDS mapping images in Figure 5b reveal that the thickness of the TiO<sub>2</sub> layer in this area is about 8 nm, which is consistent with our analysis mentioned earlier. Interestingly, a few ZnO crystallites are observed in the TiO<sub>2</sub> coating layer, and some of them even got to the surface of TiO<sub>2</sub> layer. This might be owing to the annealing process which drives some Zn atoms diffusing into the TiO<sub>2</sub> layer and forming ZnO nanocrystals. Fortunately, the presence of these ZnO nanocrystals provides more ZnO/TiO<sub>2</sub> interface, and thus enhances the beneficial effect of such interface.



**Figure 5.** (a) STEM image focus on TiO<sub>2</sub> coating layer, and its corresponding EDS mappings of (b<sub>1</sub>) O, (b<sub>2</sub>) Ti, and (b<sub>3</sub>) Zn.

X-ray diffraction (XRD) analysis was conducted to investigate the crystal structure of the ZnO nanorods, *ZT*, and *ZAT* samples. As shown in Figure 6a, all the diffraction peaks can be indexed to hexagonal wurtzite phase ZnO. The highest peak at each pattern can be indexed to the (002) planes of ZnO, indicating the nanorod growth orientation is (001). No characteristic diffraction peaks belonging to TiO<sub>2</sub> or Ag have been observed from the *ZA* and *ZAT* samples because of the very small amount or amorphous state of these materials. The peak intensity of (002) was observed increasing from ZnO to *ZT* and to *ZAT* samples, presumably due to the extra annealing step after TiO<sub>2</sub> sputtering which facilitates the crystallization of ZnO core. Figure 6b presents the X-ray photoelectron spectroscopy (XPS) spectra of Zn 2p for all four samples. No obvious change was observed for the shape of Zn peaks from these spectra, indicating that ZnO nanorods are stable in the sputtering coating and calcination process. Some small shift ( $\leq 0.5$  eV) in the peak positions is probably induced by the variation of work function among different samples. Each sputtering deposition step leads to a reduction in Zn peak intensity, which is reasonable because XPS is a surface-sensitive technique. Although no direct proof of Ag and TiO<sub>2</sub> existence could be obtained from XRD spectra, strong Ti and Ag signals can be detected from Ti 2p XPS peak (Figure 6c) of the *ZT* core-shell sample and from Ag 3p peak (Figure 6d) of *ZA* sample, respectively, indicating that TiO<sub>2</sub> and Ag have been successfully deposited on the nanorods surfaces. Furthermore, the Ti 2p<sub>3/2</sub> and 2p<sub>1/2</sub> peaks with respective binding energy of 458.7 eV and 464.4 eV indicate the formation of Ti<sup>4+</sup> in TiO<sub>2</sub> [65]. As demonstrated by the fitting for the Ag 3d peaks of the *ZA* structure, the 6.0 eV binding energy splitting of Ag 3d<sub>5/2</sub> at 368.2 eV and Ag 3d<sub>3/2</sub> at 374.2 eV indicates the Ag NPs on ZnO nanorods surfaces staying in the metallic state Ag<sup>0</sup> without oxidation [66,67].



**Figure 6.** (a) XRD patterns of the as-synthesized samples (triangle marks indicate the wurzite phase of ZnO, solid circles indicate the SnO<sub>2</sub> from the FTO glass); (b) XPS spectra of Zn 2p peaks of all four samples (ZnO, ZA, ZT, ZAT); (c,d) experimental and fitted XPS spectra and of (c) Ti 2p of ZT sample and (d) Ag 3d of ZA sample.

## 2.2. Optical and Carrier Dynamics Properties

After the structural and chemical characterizations described above, ultraviolet and visible (UV–Vis) absorption and time-resolved photoluminescence (TRPL) analysis were conducted to investigate the effects of our modifications on the optical and carrier dynamics properties. From the UV–Vis measurement data displayed in Figure 7a, we see that the Ag NPs in both the ZAT and ZTA samples can raise the light absorption, which can be partially attributed to the LSPR effect. On the other hand, the higher absorption of ZT structure in comparison with the ZnO shown in Figure 7a is probably originated from the interface states at ZnO/TiO<sub>2</sub> heterojunction. Certainly, the interface states also exist in the ZTA and ZAT samples, and together with the LSPR effect, these samples showed even higher absorption than the ZT. The similar light absorption property but highly different PEC performance between the ZAT and ZTA primarily comes from the difference in carrier recombination rate.

To further demonstrate that the ZAT structure can suppress the carrier recombination and thus extend the carrier lifetime, PL and TRPL tests were carried out on different samples that were prepared based on the ZnO nanorod arrays of similar thickness as indicated in Figure 1. Originated from the radiative recombination of carriers, the PL intensity is a measure of the product of carrier densities (i.e.,  $np$ ) in a sample as well as the rate of (radiative) recombination. Here, the PL intensities of ZT and ZAT samples are significantly lower than that of the original ZnO and ZA samples according to their PL intensity spectra for  $\lambda$  in 525–650 nm shown in Figure 7b, indicating that the carriers are separated in these structures so that their recombination are suppressed. In particular, the decay rate of the PL intensity reflects the recombination rate of carriers, which can be characterized by a parameter called carrier lifetime  $\tau$ . The normalized TRPL intensities of ZnO, ZT, ZA, and ZAT samples are plotted in Figure 7c. The PL signal of pure ZnO and ZA decays to zero in less than 200 ns. For the ZT and ZAT samples, the PL signal also drops quickly in the first stage of ~200 ns, but in the following stage the signal decays very slowly and remains at a significant intensity even after 600 ns.

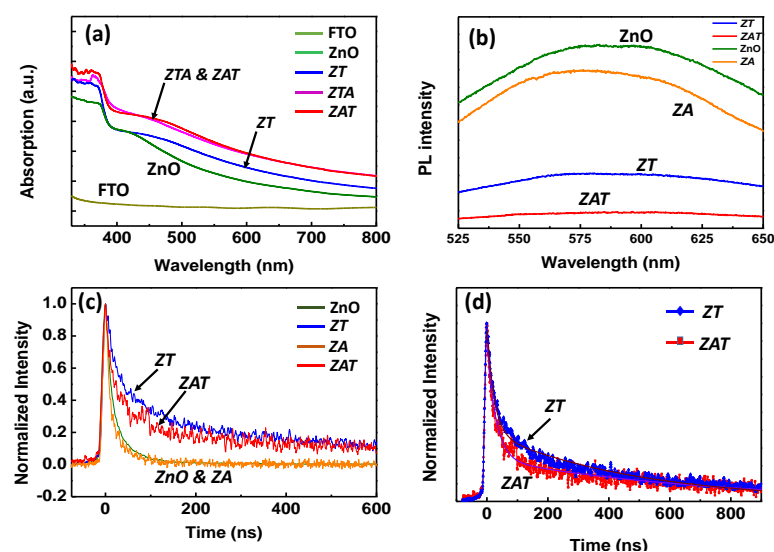


**Figure 7.** (a) UV-Vis absorption spectra of the corresponding samples; (b) Comparison of PL spectra of corresponding samples; (c) TRPL analysis of ZnO nanorod arrays, ZT, ZA, and ZAT structure with normalized intensity; (d) TRPL analysis and its fitting of ZT and ZAT structure. The excitation-lasers used in PL and TRPL tests have  $\lambda = 355$  nm, and the laser pulses with power of  $3.75 \mu\text{J}/\text{cm}^2$  were employed for the TRPL tests. The zero point of the  $y$ -axis is at the level of the  $x$ -axis in panels (a,b,d).

In order to evaluate the carrier lifetimes more accurately, we fitted the TRPL data with a multi-component decay process model [49,68–72] as the following:

$$I = \sum_i C_i \exp(-t/\tau_i), \quad (1)$$

where parameter  $\tau_i$  specifies the lifetime of the  $i$ -th decay component and  $C_i$  is the initial intensity of this component. For pure ZnO nanorod arrays and the ZA structure, there is only one quick decay process with comparable lifetime ( $\tau \sim 20$  ns) as shown in Table 1. The uncertainty of  $\tau$  in Table 1 was estimated based on the signal fluctuation and noise of the detected transient PL intensity. Besides the fast decay process with  $\tau \sim 20$  ns, another decay process with prolonged lifetime of  $\sim 490$  ns and  $700$  ns can be found in the TRPL results of ZT and ZAT samples, respectively, plotted individually in Figure 7d.

**Table 1.** Time parameter of the multi-decay process model with corresponding samples.

Sample	$\tau_1$ (ns)	$\tau_2$ (ns)
ZnO	$20 \pm 1$	-
ZA	$19 \pm 1$	-
ZT	$23 \pm 1$	$490 \pm 5$
ZAT	$29 \pm 1$	$700 \pm 5$

### 2.3. Photoelectrochemical Performance

To evaluate the effect of modified carrier dynamics on the PEC performance of these ZnO-based structures in water splitting, we first recorded the current-time transient responses as the  $I$ - $t$  curves plotted in Figure 8a,b of corresponding samples at an applied potential of  $0.4$  V versus Ag/AgCl, with chopped AM 1.5 and visible light ( $\lambda \geq 420$  nm) irradiation, respectively. Without irradiation, all the sample electrodes show small dark current ( $\leq 10^{-5}$  A/cm<sup>2</sup>, except for the ZA sample which has a dark current  $\sim 2 \times 10^{-5}$  A/cm<sup>2</sup>). Under the illumination of AM 1.5 light (which has a UV component) at a luminous power of about  $65$  mW/cm<sup>2</sup>, the good light response property of ZnO nanorods renders a significant photocurrent in every structure. Especially, the ZAT structure exhibited a photocurrent jump exceed  $5.5$  mA/cm<sup>2</sup> in each circle, indicating a photo-to-current efficiency over 25% in

the UV region. Under the visible light irradiation, only the **ZT** and **ZAT** samples exhibit relative high photocurrent (but still much lower than the cases under AM 1.5). Specifically, the **ZT** sample delivers an average photocurrent density of  $5.2 \times 10^{-5}$  A/cm<sup>2</sup>, which is 40 times larger than the current produced by pure ZnO nanorod arrays ( $\sim 1.3 \times 10^{-6}$  A/cm<sup>2</sup>). A further increase in photocurrent density ( $1.3 \times 10^{-4}$  A/cm<sup>2</sup>) is observed from the **ZAT** sample, which is about 100 times larger than that of bare ZnO sample electrode. The remarkable enhancement in PEC performances of **ZAT** and **ZT** structures is related to their long carrier lifetimes identified by the TRPL analyses discussed above.

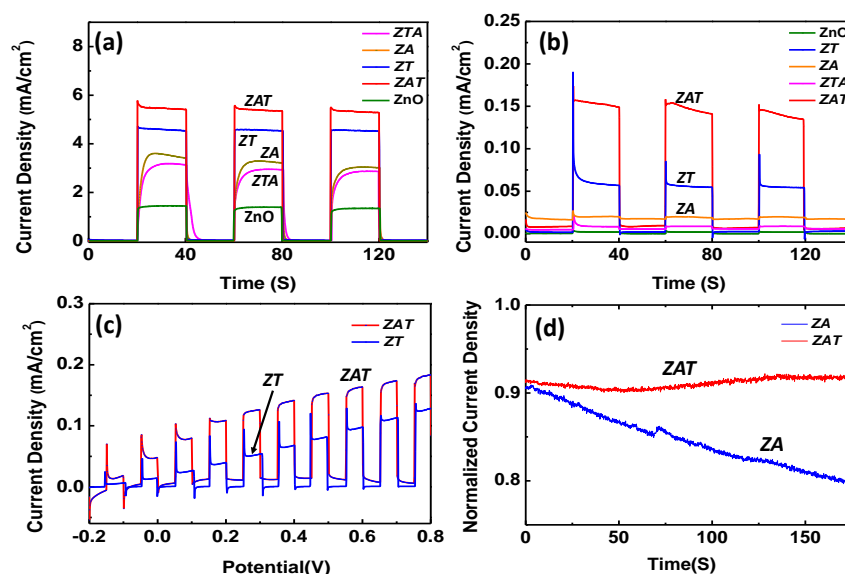


**Figure 8.** *I*-*t* curves with chopped (a) AM 1.5 light source and (b) visible light source ( $\lambda \geq 420$  nm). (c) Linear-sweep voltammograms (LSV) of heterostructures under chopped visible light illumination. (d) Comparison of the photocurrent stability of **ZAT** and **ZA** samples.

The effects of Ag NP integration can be revealed by comparing the *I*-*t* curves displayed in Figure 8a,b. In Figure 8a, under AM 1.5 irradiation, the photocurrent density increased significantly from the pure ZnO nanorods to the **ZA** samples, which could be attributed to the enhancement effect of Ag NP LSPR in the UV region. A larger photocurrent increase was observed for the **ZT** sample, which indicates that the ZnO-TiO<sub>2</sub> heterojunction and the TiO<sub>2</sub> surface termination offer a stronger enhancement effect than the Ag LSPR. The **ZTA** sample, however, generated a lower photocurrent density than the **ZT**. This suggests that the hot electrons generated by the LSPR of Ag NPs on TiO<sub>2</sub> surface cannot be consumed in (and even harmful to) the oxygen evolution reaction (OER) as the samples are used as anodes rather than cathodes in our PEC cell. Only with the Ag NPs located at the ZnO-TiO<sub>2</sub> interface, the PEC performance improved further from the **ZT** to the **ZAT** sample. Here, the effect of the Ag NP LSPR together with those of the ZnO-TiO<sub>2</sub> heterojunction and the TiO<sub>2</sub> surface termination all contribute positively to the photocurrent enhancement.

In Figure 8b, under visible ( $\lambda \geq 420$  nm) irradiation, obviously, due to the large bandgaps of the semiconductors used, the photocurrent densities of all samples are much lower than their respective counterparts in Figure 8a. Nevertheless, under visible irradiation, different factors also played their distinctive roles in PEC performance. The photocurrent density of **ZA** sample is rather low considering the dark-current background. This indicates a minor contribution of Ag NP integration just with ZnO. The significantly poorer performance of the **ZTA** sample than the **ZT** also suggests a negative effect of Ag NPs on the surface. The enhanced PEC water splitting performance of the LSPR effect was reported by Zhang et al. [73] for the Au NPs on ZnO nanorods. In that work, the Au NPs were produced on ZnO with electrochemical synthesis, so the interfacial atomic structures could be different. Furthermore, the photocurrent density with the Au-ZnO sample under a 100 mW/cm<sup>2</sup> visible ( $\lambda \geq 420$  nm) irradiation was only  $\sim 2.3 \times 10^{-5}$  A/cm<sup>2</sup>, even at 0.8 V



versus Ag/AgCl. The LSPR effect may be significant for the Au NP-ZnO sample but not for our Ag NP-ZnO. This can be explained in terms of the LSPR peak energy and shape of these plasmonic metals. The Ag-NP LSPR is sharply peaked at  $\lambda \approx 380$  nm, whereas the Au-NP LSPR is peaked at  $\lambda \approx 520$  nm and the peak is quite broad [52,74].

Although the *ZT* sample generates a relatively high photocurrent pulse immediately after the light is turned on, a significant drop of the photocurrent occurs quickly in Figure 8b. In contrast, this fast decay of the photocurrent has not been observed with the *ZAT* sample. Therefore, we further performed the linear-sweep voltammogram (LSV; shown in Figure 8c) measurement for both the *ZT* and *ZAT* samples under chopped visible light illumination. The initial decay pulse of both *ZT* and *ZAT* samples can be observed when the potential is lower than 0.2 V. When the potential is larger than 0.2 V, the pulse peak disappears in the case of *ZAT* sample. In contrast, the pulse peak appears for the *ZT* sample in each moment when light is turned on, although the amplitude of the pulse peak decreases as the potential increases. This indicates that this pulse is attributed to the recombination of photoexcited electrons and holes [75,76], therefore the height of the peak decreases because a higher potential drives electrons out of the anode more rapidly into the circuit.

Finally, we compared the stabilities of *ZAT* and *ZA* structures in the PEC process to demonstrate the function of TiO<sub>2</sub> coating also as a protection layer. In Figure 8d, we observe that the photocurrent density of *ZA* structure drops by  $\sim 12\%$  in 175 s under a constant AM 1.5 light source, probably due to the oxidation of Ag NPs on the photoanode. On the contrary, there is no drop observed of the photocurrent generated by the *ZAT* structure. Over a time scale of 1 h, the photocurrent variation of the *ZAT* sample remains in 5% range, whereas for the *ZA* sample, the decay continues, albeit at a gradually decreasing rate. Therefore, the TiO<sub>2</sub> layer strongly protected the Ag NPs from being oxidized in the PEC water splitting process.

Overall, our UV-Vis, TRPL, and PEC data indicate that the enhanced light absorption, suppression of carrier recombination at *ZT* and *ZAT* heterostructures and the TiO<sub>2</sub> surface termination play a synergetic effect in boosting the PEC activity under visible light. The LSPR of Ag NPs has no positive effect here from the comparison of the *ZT* and *ZTA* samples in Figure 8b. The Ag NPs integrated at the ZnO/TiO<sub>2</sub> interface enhanced carrier separation and extended the carrier lifetime, which are crucial to the optimal PEC performance of the *ZAT* among different samples. The *ZAT* sample has a Z-scheme layout, and the PEC performance enhancement has been observed in other Z-scheme composites [57,77,78]. In our case, as shown schematically in Figure 9, for both ZnO and TiO<sub>2</sub>, the bandgap between the conduction band minimum (CBM) and the valance band maximum (VBM) are located at about 4.3 eV and 7.5 eV below the vacuum level, respectively [13]. As the work function of silver is about 4.6 eV [79], the Fermi level of Ag NPs is  $\sim 0.3$  eV lower than the CBM of semiconductors.

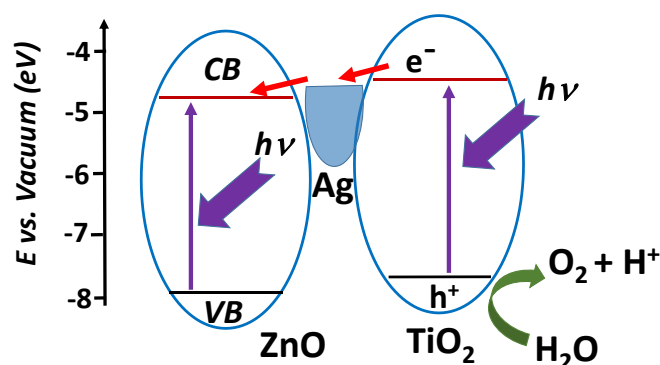


**Figure 9.** The energy levels of ZnO, Ag NP, and TiO<sub>2</sub> in the *ZAT* heterostructure, and the schematics of carrier generation, separation, and OER in TiO<sub>2</sub> in PEC water splitting. The energy levels of ZnO are pulled down more than those of other components by the positive bias voltage in the PEC system.

When the **ZAT** sample is used as a photoanode in a PEC cell, ZnO NW is connected to the positive electrode of the external power supply. Therefore, as shown in Figure 9, all energy levels will shift downward, but the amount of shift decreases consecutively from ZnO NW to Ag NP to TiO<sub>2</sub> coating. Under AM 1.5 light illumination, after electrons and holes generated in ZnO and TiO<sub>2</sub>, electrons at CBM of TiO<sub>2</sub> are more likely to transfer to Ag NPs, and further transfer to ZnO under the PEC bias. This facile electron outward transfer suppresses electron–hole recombination in the TiO<sub>2</sub> film, which significantly enhances the probability of holes participating in the OER on the TiO<sub>2</sub> surface. In the **ZA** and **ZTA** samples, the Ag NPs cannot play such a role beneficial to the OER. Instead, the Ag NPs on the surface may supply electrons that can recombine with the holes generated at VB of semiconductors, which suppresses the OER rate. This explains the observation shown in Figure 8 that **ZTA** sample has a lower PEC photocurrent density than the **ZT** sample. The exact mechanism behind the different PEC performance for our samples should be examined with further refined sample designs and carrier dynamics and energy band alignment characterizations. In addition, it is desirable to collect and quantify the hydrogen and oxygen generated in the PEC water splitting. However, such functions are not available in our current PEC testing system. These additional experiments will be performed in our future photocatalysis studies.

### 3. Materials and Methods

#### 3.1. Preparation of ZnO Nanorod Arrays

ZnO nanorod arrays were grown on fluorine-doped tin oxide-coated (FTO) glass substrates using a simple hydrothermal procedure. In detail, FTO glass substrates were first ultrasonically cleaned in acetone and deionized water, dried under N<sub>2</sub> gas flow, then loaded into the RF sputtering deposition chamber. RF power of 100 W was used to sputter the ZnO target for 25 min to obtain the ZnO seed layer. The as-prepared ZnO seed layer coated substrates then underwent a hydrothermal growth process to form ZnO nanorod arrays as reported before [33,62,63]. In the hydrothermal growth, the ZnO seed-coated FTO substrate with the coated side face-down was immersed in 0.04 M zinc nitrate (Zn(NO<sub>3</sub>)<sub>2</sub>·6H<sub>2</sub>O) solution containing hexamethylene tetraamine (HMTA) of the same concentration. The Teflon liner-containing substrates and solution were then put in a stainless-steel autoclave and heated at 95 °C for 6 h. The obtained product was then rinsed with deionized water several times followed by drying with nitrogen gas flow.

#### 3.2. Preparation of ZnO/TiO<sub>2</sub> Core-Shell Structure and Integration of Ag NPs

To prepare the **ZT** (ZnO/TiO<sub>2</sub>) and **ZTA** (ZnO/TiO<sub>2</sub>/Ag) structures, TiO<sub>2</sub> shell coating was performed through RF sputtering deposition with a RF power of 100 W for 20 min. The sample stage was heated to 450 °C during the sputtering deposition process to ensure more uniform coating. After the deposition, the TiO<sub>2</sub>-coated ZnO nanorod arrays were annealed with a hotplate in air at 450 °C for 2 h to obtain a well crystallized ZnO/TiO<sub>2</sub> core-shell structure.

To fabricate the **ZTA** heterostructure, Ag NPs integration was also performed through RF sputtering deposition, with a 75 W RF power applied to the Ag target for 2 min to deposit Ag on the surface of **ZT** at room temperature.

In order to fabricate the composite structure with Ag NPs integrated at the interface of ZnO nanorods core and TiO<sub>2</sub> shell, i.e., the **ZAT** (ZnO/Ag/TiO<sub>2</sub>) heterostructures, Ag NPs were deposited first directly on ZnO nanorods arrays through the same RF sputtering deposition to form the **ZA**, followed with TiO<sub>2</sub> coating. The coated structure was also annealed in air at 450 °C for 2 h to let ZnO core and TiO<sub>2</sub> shell crystallize better.

#### 3.3. Sample Characterization

The morphologies of the samples were investigated with field-emission SEM (FE-SEM) (JEOL-JSM-6700F, JEOL Ltd., Tokyo, Japan). The crystal structures of the samples were characterized using a BRUKER D8-Advance X-ray diffractometer (Bruker Corporation,

Billerica, MA, USA). To analyze the chemical states and surface composition of the samples, XPS was conducted with a VG ESCA system using Mg K $\alpha$  line (1253.7 eV) for excitation. TEM and HRTEM were performed using JEOL JEM-3010 (JEOL Ltd., Tokyo, Japan). STEM and EDS mapping were carried out on JEOL JEM-ARM200F (JEOL Ltd., Tokyo, Japan) attached with a large solid angle energy dispersive spectrometer (Oxford XMax100TLE EDS, Oxford Instruments, Abingdon, UK).

The TRPL spectra were collected with an Optronis Optoscope Streak Camera system (Optronis GmbH, Kehl, Germany) that has an ultimate temporal resolution of 6 ps. The wavelength  $\lambda$  and energy of excitation laser pulse is 355 nm and 3.75  $\mu\text{J}/\text{cm}^2$ , respectively. UV–Vis absorption spectra were measured with a Shimadzu UV-3600 UV–Vis–NIR spectrometer (Shimadzu Scientific Instruments, Columbia, MD, USA).

The photoelectrochemical experiments were performed in a three-electrode PEC cell, in which the working photoanode was the as-deposited sample on the FTO glass substrate, the counterelectrode is a platinum plate, and the reference electrode is aqueous Ag/AgCl/Cl $^-$ , all immersed in 0.1 M Na $_2$ SO $_4$  electrolyte. The photocurrent action spectra were measured and collected with a CHI 760 Electrochemical Workstation (CH Instruments, Inc., Austin, TX, USA). As for the light source, a 300W Xenon lamp (Perfectlight PLS-SXE300, Beijing Perfectlight Technology Co., Ltd., Beijing, China) was used, and a variety of light filters were employed to obtain desired light sources for distinct measurements. For the light source simulating the solar spectrum, an AM 1.5 solar light filter was employed. In addition, a UV cut-off ( $\lambda > 420$  nm) filter was simultaneously used with the AM 1.5 filter to simulate the visible light part of solar spectrum.

#### 4. Conclusions

In summary, we constructed ZnO/Ag/TiO $_2$  heterostructures with Ag NPs integrated at the interfaces of ZnO/TiO $_2$  core–shell nanorod arrays. The carrier lifetime and PEC activity of ZnO nanorods has been dramatically boosted by Ag NPs and TiO $_2$  coating layers. Over 30 times longer carrier lifetime has been observed in the **ZAT** structure than that in original ZnO nanorods. Correspondingly, an increase of  $\sim 100$  times in PEC photocurrent density from the original ZnO nanorod arrays to the **ZAT** Z-scheme structure was achieved with visible light source. Our PEC and TRPL tests on heterostructures assembled with different sequences, indicate that this significant boost of the PEC activity is mainly attributed to the effective carrier separation at the interface for the suppression of the recombination of photoexcited carriers, and the TiO $_2$  surface termination good for OER. The LSPR of Ag NPs enhanced the PEC performance of our samples when UV radiation component is present, but under visible light irradiation the LSPR was not present and the Ag NPs on the surface could even play a negative role. Our results presented here suggest that Z-scheme structures similar to our **ZAT** nanorod arrays should be further explored for optimal performance in practical solar energy conversion based on PEC water splitting.

**Author Contributions:** Conceptualization, Z.W. and X.-S.W.; Methodology, Z.W., T.C.S., Z.S. and X.-S.W.; Sample Preparation and Measurement, Z.W., Z.C., J.D., W.C., and C.Z.; Data Analysis, Z.W., Z.C. and W.C.; Resources, T.C.S., Z.S., X.-S.W.; Z.W. and X.-S.W. wrote and revised the article. All authors have read and agreed to the published version of the manuscript.

**Funding:** This research was funded by the Ministry of Education, Singapore, AcRF Grant R-144-000-365-112.

**Data Availability Statement:** Data are contained within the article.

**Conflicts of Interest:** The authors declare no conflict of interest.

#### References

1. Lewis, N.S.; Nocera, D.G. Powering the planet: Chemical challenges in solar energy utilization. *Proc. Natl. Acad. Sci. USA* **2006**, *103*, 15729–15735. [[CrossRef](#)] [[PubMed](#)]
2. Nozik, A.J.; Miller, J. Introduction to solar photon conversion. *Chem. Rev.* **2010**, *110*, 6443–6445. [[CrossRef](#)]

3. Cook, T.R.; Dogutan, D.K.; Reece, S.Y.; Surendranath, Y.; Teets, T.S.; Nocera, D.G. Solar energy supply and storage for the legacy and nonlegacy worlds. *Chem. Rev.* **2010**, *110*, 6474–6502. [\[CrossRef\]](#)
4. Albini, A. *Photochemistry: Past, Present and Future*; Springer: Berlin, Germany, 2016.
5. Chu, S.; Cui, Y.; Liu, N. The path towards sustainable energy. *Nat. Mater.* **2017**, *16*, 16–22. [\[CrossRef\]](#) [\[PubMed\]](#)
6. Kudo, A.; Miseki, Y. Heterogeneous photocatalyst materials for water splitting. *Chem. Soc. Rev.* **2009**, *38*, 253–278. [\[CrossRef\]](#)
7. Chen, X.; Shen, S.; Guo, L.; Mao, S.S. Semiconductor-based photocatalytic hydrogen generation. *Chem. Rev.* **2010**, *110*, 6503–6570. [\[CrossRef\]](#)
8. Ager, J.W.; Shaner, M.R.; Walczak, K.A.; Sharp, I.D.; Ardo, S. Experimental demonstrations of spontaneous, solar-driven photoelectrochemical water splitting. *Energy Environ. Sci.* **2015**, *8*, 2811–2824. [\[CrossRef\]](#)
9. Fujishima, A.; Honda, K. Electrochemical photolysis of water at a semiconductor electrode. *Nature* **1972**, *238*, 37–38. [\[CrossRef\]](#) [\[PubMed\]](#)
10. Liu, C.; Dasgupta, N.P.; Yang, P. Semiconductor nanowires for artificial photosynthesis. *Chem. Mater.* **2014**, *26*, 415–422. [\[CrossRef\]](#)
11. Polman, A.; Knight, M.; Garnett, E.C.; Ehrler, B.; Sinke, W.C. Photovoltaic materials: Present efficiencies and future challenges. *Science* **2016**, *352*, 307. [\[CrossRef\]](#)
12. Hunter, B.M.; Gray, H.B.; Müller, A.M. Earth-abundant heterogeneous water oxidation catalysts. *Chem. Rev.* **2016**, *116*, 14120–14136. [\[CrossRef\]](#)
13. Hoang, S.; Gao, P.-X. Nanowire array structures for photocatalytic energy conversion and utilization: A review of design concepts, assembly and integration, and function enabling. *Adv. Energy Mater.* **2016**, *6*, 1600683. [\[CrossRef\]](#)
14. Montoya, J.H.; Seitz, L.C.; Chakthranont, P.; Vojvodic, A.; Jaramillo, T.F.; Nørskov, J.K. Materials for solar fuels and chemicals. *Nat. Mater.* **2017**, *16*, 70–81. [\[CrossRef\]](#)
15. Chu, S.; Li, W.; Yan, Y.; Hamann, T.; Shih, I.; Wang, D.; Mi, Z. Roadmap on solar water splitting: Current status and future prospects. *Nano Futures* **2017**, *1*, 022001. [\[CrossRef\]](#)
16. Petronella, F.; Comparelli, R. Nanomaterials in photo (electro) catalysis. *Catalysts* **2021**, *11*, 149. [\[CrossRef\]](#)
17. Ibadurrohmam, M.; Hellgardt, K. Morphological modification of TiO<sub>2</sub> thin films as highly efficient photoanodes for photoelectrochemical water splitting. *ACS Appl. Mater. Interfaces* **2015**, *7*, 9088–9097. [\[CrossRef\]](#)
18. Etacheri, V.; Di Valentin, C.; Schneider, J.; Bahnemann, D.; Pillai, S.C. Visible-light activation of TiO<sub>2</sub> photocatalysts: Advances in theory and experiments. *J. Photochem. Photobiol. C* **2015**, *25*, 1–29. [\[CrossRef\]](#)
19. Wettstein, C.M.; Sánchez, C.G. Characterization of ZnO as substrate for DSSC. *Phys. Chem. Chem. Phys.* **2018**, *20*, 21910–21916. [\[CrossRef\]](#)
20. De Pasquale, I.; Lo Porto, C.; Dell'Edera, M.; Petronella, F.; Agostiano, A.; Curri, M.L.; Comparelli, R. Photocatalytic TiO<sub>2</sub>-based nanostructured materials for microbial inactivation. *Catalysts* **2020**, *10*, 1382. [\[CrossRef\]](#)
21. Kubacka, A.; Fernández-García, M.; Colón, G. Advanced nanoarchitectures for solar photocatalytic applications. *Chem. Rev.* **2011**, *112*, 1555–1614. [\[CrossRef\]](#)
22. Li, X.; Yu, J.; Jaroniec, M. Hierarchical photocatalysts. *Chem. Soc. Rev.* **2016**, *45*, 2603–2636. [\[CrossRef\]](#)
23. Li, X.; Yu, J.; Low, J.; Fang, Y.; Xiao, J.; Chen, X. Engineering heterogeneous semiconductors for solar water splitting. *J. Mater. Chem. A* **2015**, *3*, 2485–2534. [\[CrossRef\]](#)
24. Luo, J.; Zhang, S.; Sun, M.; Yang, L.; Luo, S.; Crittenden, J.C. A critical review on energy conversion and environmental remediation of photocatalysts with remodeling crystal lattice, surface, and interface. *ACS Nano* **2019**, *13*, 9811–9840. [\[CrossRef\]](#)
25. Tang, R.; Zhou, S.; Zhang, Z.; Zheng, R.; Huang, J. Engineering nanostructure–interface of photoanode materials toward photoelectrochemical water oxidation. *Adv. Mater.* **2021**, *33*, 2005389. [\[CrossRef\]](#) [\[PubMed\]](#)
26. Myung, Y.; Jang, D.M.; Sung, T.K.; Sohn, Y.J.; Jung, G.B.; Cho, Y.J.; Kim, H.S.; Park, J. Composition-tuned ZnO–CdSSe core-shell nanowire arrays. *ACS Nano* **2010**, *4*, 3789–3800. [\[CrossRef\]](#) [\[PubMed\]](#)
27. Wang, R.; Xu, X.; Zhang, Y.; Chang, Z.; Sun, Z.; Dong, W.-F. Functionalized ZnO@TiO<sub>2</sub> nanorod array film loaded with ZnIn<sub>0.25</sub>Cu<sub>0.02</sub>S<sub>1.395</sub> solid-solution: Synthesis, characterization and enhanced visible light driven water splitting. *Nanoscale* **2015**, *7*, 11082–11092. [\[CrossRef\]](#)
28. Kwiatkowski, M.; Chassagnon, R.; Heintz, O.; Geoffroy, N.; Skompska, M.; Bezverkhyy, I. Improvement of photocatalytic and photoelectrochemical activity of ZnO/TiO<sub>2</sub> core/shell system through additional calcination: Insight into the mechanism. *Appl. Catal. B Environ.* **2017**, *204*, 200–208. [\[CrossRef\]](#)
29. Mansournia, M.; Ghaderi, L. CuO@ZnO core-shell nanocomposites: Novel hydrothermal synthesis and enhancement in photocatalytic property. *J. Alloys Compd.* **2017**, *691*, 171–177. [\[CrossRef\]](#)
30. Guo, H.; Su, C.; Yu, D.; Li, L.; Liu, Z.; Han, Z.; Lu, X. Facile fabrication of ZnO/CuS heterostructure photoanode with highly PEC performance and excellent charge separation efficiency. *J. Electroanal. Chem.* **2019**, *854*, 113546. [\[CrossRef\]](#)
31. Jia, S.; Li, X.; Zhang, B.; Yang, J.; Zhang, S.; Li, S.; Zhang, Z. TiO<sub>2</sub>/CuS heterostructure nanowire array photoanodes toward water oxidation: The role of CuS. *Appl. Surf. Sci.* **2019**, *463*, 829–837. [\[CrossRef\]](#)
32. Zhang, T.; Lin, P.; Wei, N.; Wang, D. Enhanced photoelectrochemical water-splitting property on TiO<sub>2</sub> nanotubes by surface chemical modification and wettability control. *ACS Appl. Mater. Interfaces* **2020**, *12*, 20110–20118. [\[CrossRef\]](#)
33. Wang, T.; Jiao, Z.; Chen, T.; Li, Y.; Ren, W.; Lin, S.; Lu, G.; Ye, J.; Bi, Y. Vertically aligned ZnO nanowire arrays tip-grafted with silver nanoparticles for photoelectrochemical applications. *Nanoscale* **2013**, *5*, 7552–7557. [\[CrossRef\]](#)



34. Hu, J.; You, N.; Yu, Z.; Zhou, G.; Xu, X. Two-dimensional ZnO ultrathin nanosheets decorated with Au nanoparticles for effective photocatalysis. *J. Appl. Phys.* **2016**, *120*, 074301. [\[CrossRef\]](#)
35. Mishra, P.; Patnaik, S.; Parida, K. An overview of recent progress on noble metal modified magnetic Fe<sub>3</sub>O<sub>4</sub> for photocatalytic pollutant degradation and H<sub>2</sub> evolution. *Catal. Sci. Technol.* **2019**, *9*, 916–941. [\[CrossRef\]](#)
36. Chen, B.; Chen, X.; Li, R.; Fan, W.; Wang, F.; Mao, B.; Shi, W. Flame reduced TiO<sub>2</sub> nanorod arrays with Ag nanoparticle decoration for efficient solar water splitting. *Ind. Eng. Chem. Res.* **2019**, *58*, 4818–4827. [\[CrossRef\]](#)
37. Wint, T.H.M.; Smith, M.F.; Chanlek, N.; Chen, F.; Oo, T.Z.; Songsiririthigul, P. Physical origin of diminishing photocatalytic efficiency for recycled TiO<sub>2</sub> nanotubes and Ag-loaded TiO<sub>2</sub> nanotubes in organic aqueous solution. *Catalysts* **2020**, *10*, 737. [\[CrossRef\]](#)
38. Reñones, P.; Collado, L.; Iglesias-Juez, A.; Oropeza, F.E.; Fresno, F.; de la Peña O'Shea, V.A. Silver–gold bimetal-loaded TiO<sub>2</sub> photocatalysts for CO<sub>2</sub> reduction. *Ind. Eng. Chem. Res.* **2020**, *59*, 9440–9450. [\[CrossRef\]](#)
39. Thalluri, S.M.; Bai, L.; Lv, C.; Huang, Z.; Hu, X.; Liu, L. Strategies for semiconductor/electrocatalyst coupling toward solar-driven water splitting. *Adv. Sci.* **2020**, *7*, 1902102. [\[CrossRef\]](#) [\[PubMed\]](#)
40. Lee, S.Y.; Kang, D.; Jeong, S.; Do, H.T.; Kim, J.H. Photocatalytic degradation of rhodamine B dye by TiO<sub>2</sub> and gold nanoparticles supported on a floating porous polydimethylsiloxane sponge under ultraviolet and visible light irradiation. *ACS Omega* **2020**, *5*, 4233–4241. [\[CrossRef\]](#) [\[PubMed\]](#)
41. Shiraishi, Y.; Toi, S.; Ichikawa, S.; Hirai, T. Photocatalytic NH<sub>3</sub> splitting on TiO<sub>2</sub> particles decorated with Pt–Au bimetallic alloy nanoparticles. *ACS Appl. Nano Mater.* **2020**, *3*, 1612–1620. [\[CrossRef\]](#)
42. Singh, S.V.; Kumar, M.P.; Anantharaj, S.; Mukherjee, B.; Kundu, S.; Pal, B.N. Direct evidence of an efficient plasmon-induced hot-Electron transfer at an in situ grown Ag/TiO<sub>2</sub> interface for highly enhanced solar H<sub>2</sub> generation. *ACS Appl. Energy Mater.* **2020**, *3*, 1821–1830. [\[CrossRef\]](#)
43. Liu, M.; Chen, Y.; Su, J.; Shi, J.; Wang, X.; Guo, L. Photocatalytic hydrogen production using twinned nanocrystals and an unanchored NiS<sub>x</sub> co-catalyst. *Nat. Energy* **2016**, *1*, 16151. [\[CrossRef\]](#)
44. Kumar, S.G.; Devi, L.G. Review on modified TiO<sub>2</sub> photocatalysis under UV/visible light: Selected results and related mechanisms on interfacial charge carrier transfer dynamics. *J. Phys. Chem. A* **2011**, *115*, 13211–13241. [\[CrossRef\]](#) [\[PubMed\]](#)
45. Ponseca, C.S., Jr.; Chábera, P.; Uhlig, J.; Persson, P.; Sundström, V. Ultrafast electron dynamics in solar energy conversion. *Chem. Rev.* **2017**, *117*, 10940–11024. [\[CrossRef\]](#)
46. Arkan, F.; Izadyar, M.; Nakhaeipour, A. Improvement in charge transfer dynamic of the porphyrin-based solar cells in water: A theoretical study. *J. Renew. Sustain. Energy* **2017**, *9*, 023502. [\[CrossRef\]](#)
47. Eichhorn, J.; Kastl, C.; Cooper, J.K.; Ziegler, D.; Schwartzberg, A.M.; Sharp, I.D.; Toma, F.M. Nanoscale imaging of charge carrier transport in water splitting photoanodes. *Nat. Commun.* **2018**, *9*, 2597. [\[CrossRef\]](#) [\[PubMed\]](#)
48. Singhal, P.; Ghosh, H.N. Hot charge carrier extraction from semiconductor quantum dots. *J. Phys. Chem. C* **2018**, *122*, 17586–17600. [\[CrossRef\]](#)
49. Utterback, J.K.; Wilker, M.B.; Mulder, D.W.; King, P.W.; Eaves, J.D.; Dukovic, G. Quantum efficiency of charge transfer competing against nonexponential processes: The case of electron transfer from CdS nanorods to hydrogenase. *J. Phys. Chem. C* **2019**, *123*, 886–896. [\[CrossRef\]](#)
50. Rafiq, S.; Scholes, G.D. From fundamental theories to quantum coherences in electron transfer. *J. Am. Chem. Soc.* **2019**, *141*, 708–722. [\[CrossRef\]](#) [\[PubMed\]](#)
51. Baffou, G.; Quidant, R. Nanoplasmonics for chemistry. *Chem. Soc. Rev.* **2014**, *43*, 3898–3907. [\[CrossRef\]](#)
52. Jiang, R.; Li, B.; Fang, C.; Wang, J. Metal/semiconductor hybrid nanostructures for plasmon-enhanced applications. *Adv. Mater.* **2014**, *26*, 5274–5309. [\[CrossRef\]](#)
53. Smith, J.G.; Faucheaux, J.A.; Jain, P.K. Plasmon resonances for solar energy harvesting: A mechanistic outlook. *Nano Today* **2015**, *10*, 67–80. [\[CrossRef\]](#)
54. Su, Y.-H.; Ke, Y.-F.; Cai, S.-L.; Yao, Q.-Y. Surface plasmon resonance of layer-by-layer gold nanoparticles induced photoelectric current in environmentally-friendly plasmon-sensitized solar cell. *Light Sci. Appl.* **2012**, *1*, e14. [\[CrossRef\]](#)
55. Zhang, Y.; He, S.; Guo, W.; Hu, Y.; Huang, J.; Mulcahy, J.R.; Wei, W.D. Surface-plasmon-driven hot electron photochemistry. *Chem. Rev.* **2018**, *118*, 2927–2954. [\[CrossRef\]](#) [\[PubMed\]](#)
56. Low, J.; Jiang, C.; Cheng, B.; Wageh, S.; Al-Ghamdi, A.A.; Yu, J. A review of direct Z-scheme photocatalysts. *Small Methods* **2017**, *1*, 1700080. [\[CrossRef\]](#)
57. Maeda, K. Z-scheme water splitting using two different semiconductor photocatalysts. *ACS Catal.* **2013**, *3*, 1486–1503. [\[CrossRef\]](#)
58. Wang, Y.; Kong, X.; Jiang, M.; Zhang, F.; Lei, X. A Z-scheme ZnIn<sub>2</sub>S<sub>4</sub>/Nb<sub>2</sub>O<sub>5</sub> nanocomposite: Constructed and used as an efficient bifunctional photocatalyst for H<sub>2</sub> evolution and oxidation of 5-hydroxymethylfurfural. *Inorg. Chem. Front.* **2020**, *7*, 437–446. [\[CrossRef\]](#)
59. Lin, Y.; Zhang, Q.; Li, Y.; Liu, Y.; Xu, K.; Huang, J.; Zhou, X.; Peng, F. The evolution from a typical Type-I CdS/ZnS to Type-II and Z-scheme hybrid structure for efficient and stable hydrogen production under visible light. *ACS Sustain. Chem. Eng.* **2020**, *8*, 4537–4546. [\[CrossRef\]](#)
60. Maarisetty, D.; Mahanta, S.; Sahoo, A.K.; Mohapatra, P.; Baral, S.S. Steering the charge kinetics in dual-functional photocatalysis by surface dipole moments and band edge modulation: A defect study in TiO<sub>2</sub>-ZnS-rGO composites. *ACS Appl. Mater. Interfaces* **2020**, *12*, 11679–11692. [\[CrossRef\]](#) [\[PubMed\]](#)

61. Wang, M.; Huang, C.; Cao, Y.; Yu, Q.; Guo, W.; Liu, Q.; Liang, J.; Hong, M. A plasma sputtering decoration route to producing thickness-tunable ZnO/TiO<sub>2</sub> core/shell nanorod arrays. *Nanotechnology* **2009**, *20*, 285311. [\[CrossRef\]](#)
62. Dev, A.; Panda, S.K.; Kar, S.; Chakrabarti, S.; Chaudhuri, S. Surfactant-assisted route to synthesize well-aligned ZnO nanorod arrays on sol–gel-derived ZnO thin films. *J. Phys. Chem. B* **2006**, *110*, 14266–14272. [\[CrossRef\]](#)
63. Greene, L.E.; Law, M.; Goldberger, J.; Kim, F.; Johnson, J.C.; Zhang, Y.; Saykally, R.J.; Yang, P. Low-temperature wafer-scale production of ZnO nanowire arrays. *Angew. Chem. Int. Ed.* **2003**, *42*, 3031–3034. [\[CrossRef\]](#)
64. Han, H.; Wang, W.; Yao, L.; Hao, C.; Liang, Y.; Fu, J.; Zeng, P. Photostable 3D heterojunction photoanode made of ZnO nanosheets coated onto TiO<sub>2</sub> nanowire arrays for photoelectrochemical solar hydrogen generation. *Catal. Sci. Technol.* **2019**, *9*, 1989–1997. [\[CrossRef\]](#)
65. Ma, L.; Huang, Y.; Hou, M.; Xie, Z.; Zhang, Z. Ag nanorods coated with ultrathin TiO<sub>2</sub> shells as stable and recyclable SERS substrates. *Sci. Rep.* **2015**, *5*, 15442. [\[CrossRef\]](#) [\[PubMed\]](#)
66. Rakibuddin, M.; Ananthakrishnan, R. A novel Ag deposited nanocoordination polymer derived porous SnO<sub>2</sub>/NiO hetero-nanostructure for the enhanced photocatalytic reduction of Cr(VI) under visible light. *New J. Chem.* **2016**, *40*, 3385–3394. [\[CrossRef\]](#)
67. Zhang, H.; Wang, G.; Chen, D.; Lv, X.; Li, J. Tuning photoelectrochemical performances of Ag-TiO<sub>2</sub> nanocomposites via reduction/oxidation of Ag. *Chem. Mater.* **2008**, *20*, 6543–6549. [\[CrossRef\]](#)
68. Demas, J.N. *Excited State Lifetime Measurements*; Academic Press: New York, NY, USA, 1983.
69. Kuciauskas, D.; Duenow, J.N.; Kanevce, A.; Li, J.V.; Young, M.R.; Dippo, P.; Levi, D.H. Optical-fiber-based, time-resolved photoluminescence spectrometer for thin-film absorber characterization and analysis of TRPL data for CdS/CdTe interface. In Proceedings of the 2012 38th IEEE Photovoltaic Specialists Conference, Austin, TX, USA, 3–8 June 2012; pp. 001721–001726.
70. Malik, M.A.; O'brien, P.; Norager, S.; Smith, J. Gallium arsenide nanoparticles: Synthesis and characterisation. *J. Mater. Chem.* **2003**, *13*, 2591–2595. [\[CrossRef\]](#)
71. Chen, X.; Wang, K.; Beard, M.C. Ultrafast probes at the interfaces of solar energy conversion materials. *Phys. Chem. Chem. Phys.* **2019**, *21*, 16399–16407. [\[CrossRef\]](#)
72. Lai, T.-H.; Katsumata, K.-I.; Hsu, Y.-J. In situ charge carrier dynamics of semiconductor nanostructures for advanced photoelectrochemical and photocatalytic applications. *Nanophotonics* **2020**, *10*, 777–795. [\[CrossRef\]](#)
73. Zhang, W.; Wang, W.; Shi, H.; Liang, Y.; Fu, J.; Zhu, M. Surface plasmon-driven photoelectrochemical water splitting of aligned ZnO nanorod arrays decorated with loading-controllable Au nanoparticles. *Sol. Energy Mater. Sol. Cells* **2018**, *180*, 25–33. [\[CrossRef\]](#)
74. Jain, P.K.; El-Sayed, M.A. Plasmonic coupling in noble metal nanostructures. *Chem. Phys. Lett.* **2010**, *487*, 153–164. [\[CrossRef\]](#)
75. Peter, L.M. Dynamic aspects of semiconductor photoelectrochemistry. *Chem. Rev.* **1990**, *90*, 753–769. [\[CrossRef\]](#)
76. Choi, S.K.; Choi, W.; Park, H. Solar water oxidation using nickel-borate coupled BiVO<sub>4</sub> photoelectrodes. *Phys. Chem. Chem. Phys.* **2013**, *15*, 6499–6507. [\[CrossRef\]](#) [\[PubMed\]](#)
77. Fu, J.; Cao, S.; Yu, J. Dual Z-scheme charge transfer in TiO<sub>2</sub>–Ag–Cu<sub>2</sub>O composite for enhanced photocatalytic hydrogen generation. *J. Mater. Chem.* **2015**, *1*, 124–133. [\[CrossRef\]](#)
78. Hisatomi, T.; Kubota, J.; Domen, K. Recent advances in semiconductors for photocatalytic and photoelectrochemical water splitting. *Chem. Soc. Rev.* **2014**, *43*, 7520–7535. [\[CrossRef\]](#)
79. Dweydari, A.W.; Mee, C.H.B. Work function measurements on (100) and (110) surfaces of silver. *Phys. Status Solidi A* **1975**, *27*, 223–230. [\[CrossRef\]](#)